Marine Heatwaves in the Red Sea and their Relationship to Different Climate Modes: A Case Study of the 2010 Events in the Northern Red Sea

Manal Hamdeno[1,2], Aida Alvera-Azcárate[1], George Krokos[3,4], Ibrahim Hoteit[3]

5   [1]GeoHydrodynamics and Environment Research (GHER), University of Liège, Liège, Belgium
[2]Oceanography Department, Faculty of Science, Alexandria University, Alexandria, Egypt
[3]Physical Sciences and Engineering Division, King Abdullah University of Science and Technology (KAUST), Thuwal, Saudi Arabia
[4]Institute of Oceanography, Hellenic Centre for Marine Research, Anavyssos, Greece,

10   *Correspondence to*: Manal Hamdeno (mh.elawady@uliege.be)

Abstract.

In the context of climate change, the oceans are progressively warming, leading to an increase in the occurrence of marine heatwaves (MHWs). This warming trend is particularly striking in the Red Sea and has a significant impact on its ecosystem. The current study focuses on the characteristics of MHWs in the Red Sea in recent decades and examines their spatial

15   patterns in the Red Sea sub-regions. In addition, the relationships between MHWs frequency and different climate modes are investigated. The extreme MHW events that occurred in the northern region in 2010 were analyzed. Through the analysis of satellite-derived sea surface temperatures (SST), a warming trend was observed that began in 1994 and has intensified significantly since 2016. This rise in temperature is accompanied by an increase in the frequency and total number of MHW days in the basin. In the last four decades (1982-2021), there have been 78 MHW events with a total of 1016 heat days. It is

20   noteworthy that 46% of the events and 58% of the heat days occurred in the last decade. The spatial analysis of MHW characteristics in the Red Sea shows high variability, with longer and more intense MHWs occurring in the northern Red Sea (NRS), while they were more frequent in the southern Red Sea (SRS). The annual MHW frequency in the NRS peaked in 2010, 2018, 2019 and 2021, while it was highest in the SRS in 1998 and from 2017 to 2021. When comparing the annual mean values of atmospheric variables with the annual frequency of MHWs, a correlation was found. It was observed that

25   years characterized by an increased frequency of MHWs coincided with anomalously high total heat fluxes and air temperatures, while exhibiting anomalously low wind speeds. This relationship was particularly pronounced in the NRS in 2010 and in the SRS in 1998. A link is then established between the SST anomaly, the MHW frequency and certain climate indices. The Atlantic Multidecadal Oscillation (AMO) and the Indian Ocean Dipole (IOD) showed a positive spatial correlation with the SSTA and the MHW frequency. In contrast, the East Atlantic/West Russian pattern (EATL/WRUS)

30   showed a negative correlation with the SSTA and the MHW frequency, especially in the NRS. The MHWs of 2010 were further investigated as it was one of the warmest years in our study period, which had highly frequent MHWs with a different spatial distribution than the other warm years. It was also observed that the AMO and IOD were in a robust positive phase in 2010, while the EATL/WRUS and North Atlantic Oscillation (NAO) were in their most pronounced negative phase, which may have contributed to the increased occurrence of MHWs in that year. This study highlights the link between

35   climate indices, atmospheric conditions and the occurrence of marine heatwaves in the Red Sea and provides valuable insights into this critical aspect of climate change.

1 Introduction

Episodes of very warm sea surface temperature (SST) anomalies, known as "marine heatwaves" (MHWs), have been observed in all the world's oceans and marginal seas and have increased in frequency and duration in the recent decades
40 (Hobday et al., 2016, 2018; Oliver et al., 2018, 2021; Holbrook et al., 2020; Sen Gupta et al., 2020). These extreme warm water events can be triggered by atmospheric forcings, oceanic processes, or a combination of both, and these drivers can vary based on season and geographic location (Holbrook et al., 2019; Amaya et al., 2020; Sen Gupta et al., 2020; Mohamed et al., 2021; Oliver et al., 2021; Pujol et al., 2022). MHWs have ecological and socioeconomic impacts, including coral bleaching (Eakin et al., 2010; Hughes et al., 2018; Genevier et al., 2019), declines in sea surface productivity (Le Grix et al.,
45 2021; Hamdeno et al., 2022; Hamdeno and Alvera-Azcaráte, 2023), mortality of benthic communities (Garrabou et al., 2009; Smale and Wernberg, 2009; Rivetti et al., 2014), and loss of seagrass beds (Diaz-Almela et al., 2007; Carlson et al., 2018; Chefaoui et al., 2018) and kelp forests (Arafeh-Dalmau et al., 2019).

The Red Sea is a semi-enclosed, elongated marginal sea between Africa and Asia, connected to the Indian Ocean on the south by the Strait of Bab-al-Mandeb and to the Mediterranean Sea on the north by the Suez Canal (Figure 1). Due to their
50 small volume and slow rate of water renewal, marginal, semi-enclosed seas such as the Red Sea are particularly vulnerable to global warming (Krokos et al., 2019). The Red Sea has an arid climate and a negative water balance, i.e. evaporation exceeds precipitation and river runoff combined (Bower and Farrar, 2015; Eladawy et al., 2017; Liu and Yao, 2022). The Red Sea is of critical political and economic importance locally and globally, as it is a vital resource for fisheries, agriculture, tourism, and freshwater production through desalination, and is a major shipping route (Barale, 2014; Krokos et
55 al., 2019; Hoteit et al., 2021).

Due to the importance of the Red Sea, several studies have investigated its physical properties, especially SST, as it can serve as an indicator of the thermal stress caused by global warming, which has devastating effects on the rich and diverse marine life of the Red Sea (Raitsos et al., 2011; Barros et al., 2014; Chaidez et al., 2017; Karnauskas and Jones, 2018; Shaltout, 2019; Trisos et al., 2020; Liu and Yao, 2022). However, only a few studies that have investigated MHWs in the
60 Red Sea (Genevier et al., 2019; Bawadekji et al., 2021; Mohamed et al., 2021), and up-to-date there are no studies have investigated the link between climate patterns and the occurrence of MHWs in the Red Sea region. Raitsos et al. (2011) used satellite-derived SST to examine the spatiotemporal changes in Red Sea temperatures between 1985 and 2007 and concluded that the Red Sea is experiencing a strong warming that began in the mid-1990s and increased abruptly after 1994. Another study by Chaidez et al. (2017) calculated the warming trends in the Red Sea between 1982 and 2015 and estimated the
65 overall rate of warming for the Red Sea to be 0.17 ± 0.07 °C/decade, while the SST trend in the northern Red Sea was between 0.40 and 0.45 °C/decade, which is higher than the global rate. According to the IPCC, the Red Sea is warming due to climate change and a temperature rise of 3.45 °C is expected for the period 2010-2099 (Barros et al., 2014; Trisos et al., 2020). A recent study by Liu and Yao (2022) examined the long-term variations in the SST of the Red Sea and adjacent seas, as well as surface air temperatures, from 1875 to 2019. They found that the SST of the Red Sea increased at an average rate

70   of 0.43 °C/decade during these years, and this rate has accelerated in recent decades. Furthermore, they found that the SST anomalies of the Red Sea are positively correlated and strongly synchronized with those of the adjacent seas and with air temperature anomalies.

Genevier et al. (2019) established a link between the MHWs and coral bleaching in the Red Sea during the summer months (July-October). Using satellite sea surface temperature (SST) data from 1985 to 2015, they found that MHWs in the Red Sea

75   can trigger coral bleaching when their SSTs exceed the 95th percentile, when the climatological average is 30°C or higher, last for at least seven consecutive days and occur at shallow depths (< 150 m). Bawadekji et al. (2021) studied the general and local characteristics of the marine heatwaves in the Red Sea. Their study concluded that the Red Sea exhibits a meridional gradient with decreasing average annual MHW intensity and MHW duration from north to south, and a meridional gradient with increasing average annual MHW frequency from north to south. Finally, Mohamed et al. (2021)

80   studied the spatio-temporal variability and trends of MHWs in the Red Sea over 39 years (1982-2020) using high-resolution satellite SST data. Their results showed that over the last two decades (2000 – 2020), the average frequency and duration of heatwaves increased by 35% and 67%, respectively. Their study also showed that the highest annual MHW frequencies were recorded in 2010, 2017, 2018, and 2019.

It is well known that the oceans are the main drivers of internal climate variability, affecting climate around the world (e.g.,

85   Shukla, 1998). Many modes of climate variability are coupled ocean-atmosphere phenomena, such as the El Nino-Southern Oscillation (ENSO), which is the most important mode of global climate variability on interannual time scales (e.g., McPhaden et al., 2006). At the local scale, it has long been known that the broader region surrounding the Red Sea is directly influenced by the North Atlantic Oscillation (NAO) (Visbeck et al., 2001), and the Atlantic Multidecadal Oscillation (AMO) (Krokos et al., 2019), while ENSO is known to indirectly influence the neighboring tropical Indian Ocean via atmospheric

90   teleconnections (Bjerknes, 1969). In this paper, we will examine the annual variability of SST and MHWs un the Red Sea and its relationship to the AMO, Indian Ocean Dipole (IOD), The East Atlantic/ West Russia (EATL/WRUS) pattern, NAO, and Oceanic Niño Index (ONI).

The AMO was identified as a coherent mode of natural variability in the North Atlantic with an estimated duration of 60-80 years. It is based on average sea surface temperature (SST) anomalies in the North Atlantic basin, typically over 0° – 80° N.

95   The positive AMO phase corresponds with positive SST anomalies over most of the North Atlantic, with stronger anomalies in the subpolar region and weaker anomalies in the tropics. It has significant regional and hemispheric impacts on climate, such as the Northern Hemisphere mean surface temperature (Zhang, 2007; Semenov et al., 2010; Schneider et al., 2013). The IOD is a climate phenomenon that occurs in the Indian Ocean, and is defined as the difference in SST between the eastern and western regions of the Indian Ocean. The IOD can significantly affect weather patterns and climate in surrounding

100   regions, including parts of Africa, Southeast Asia, and Australia. During a positive phase, warm water is pushed into the western part of the Indian Ocean, while cold deep water rises to the surface in the eastern Indian Ocean and vice during the negative phase (Behera et al., 2021; Cai et al., 2021). The EATL/WRUS pattern is one of three prominent teleconnection patterns that affect Eurasia throughout the year. The major surface temperature anomalies associated with the positive phase

of the EATL/WRUS pattern reflect above-average temperatures over East Asia and below-average temperatures over much of western Russia and northeastern Africa (Barnston and Livezey, 1987). The NAO index is based on the sea level pressure difference between the subtropical high (Azores) and the subpolar low. Strong positive phases of the NAO are usually accompanied by above-average temperatures in the eastern United States and northern Europe and below-average temperatures in Greenland and often in southern Europe and the Middle East (Barnston and Livezey, 1987; Dool et al., 2000; Chen and Dool, 2003). ONI is a primary indicator for monitoring El Niño and La Niña, which are opposite phases of the climate pattern called El Niño-Southern Oscillation "ENSO". ONI is the difference between a three-month running average of sea surface temperature averaged over an ocean area between 120° W and 170° W along the equator and the long-term average for the same three months. El Niño conditions are considered to exist when the Oceanic Niño Index is +0.5 or higher, meaning that the eastern and central tropical Pacific Ocean is significantly warmer than normal. La Niña conditions are present when the Oceanic Niño Index is -0.5 or lower, meaning that the region is cooler than normal (Bamston et al., 1997; Hoerling et al., 2001; McPhaden et al., 2006; Huang et al., 2017)

The main objectives of the current work is to investigate the spatiotemporal variability of MHW characteristics over the Red Sea (RS) and to assess the difference between these characteristics in the northern (NRS) and southern (SRS) regions of the RS. The study also aims to investigate the correlations between the different climate modes with the annual sea surface temperature anomaly (SSTA) and the annual frequency of MHWs in the Red Sea. The work is divided into four sections; Section one: SST and MHW characteristics and trends in the RS between 1982 and 2021; Section two: the interannual variability of SSTA and MHW over the last four decades in the RS and its northern and southern basins; Section three: the relationship between SSTA/MHW of the RS and the different climate modes; Section four: the 2010 MHW events in the NRS as a case study.

2 Data and Methods of Analysis

2.1 Datasets

To analyze the spatial and temporal variability of SST and MHWs in the Red Sea and examinee their interactions with different climate modes, focusing on the 2010 MHW events as a case study, various available data sources are used:

i- Red Sea bathymetry was obtained from GEBCO's current bathymetric dataset, the GEBCO_2023 Grid (https://www.gebco.net/data_and_products/gridded_bathymetry_data/). This is a global terrain model for ocean and land that provides elevation data in meters on a grid with an interval of 15 arc-seconds (Schenke, 2013). The bathymetry of the Red Sea was extracted from the global bathymetry map.

ii- Daily high-resolution SST data from January 1, 1982 to December 31, 2021 obtained from the Copernicus Marine Environment Monitoring Service (CMEMS; https://data.marine.copernicus.eu/product/SST_GLO_SST_L4_REP_OBSERVATIONS_010_011/description) website. The CMEMS Operational SST and Ice Analysis (OSTIA) reprocessed analysis product is based on an SST

satellite and in situ observation (Good et al., 2020). The SST dataset consists of daily, gapless maps of SST and ice concentration (referred to as the L4 product) with a horizontal grid resolution of $0.05° \times 0.05°$.

140   iii- Hourly mixed layer depth (MLD) and water column temperature are obtained from a regionally tuned simulation of the MIT general circulation model (MITgcm; Marshall et al., 1997) with a horizontal resolution of 1 km and 50 vertical layers (Krokos et al., 2021). The model domain covers the entire Red Sea, including the two Gulfs (Suez and Aqaba) at the northern end, with an open boundary in the Gulf of Aden. The topography of the model is based on the General Bathymetric Map of the Ocean (Weatherall et al., 2015) updated with available regional data. The

145   model is driven with hourly, high-resolution (~5km) atmospheric downscaled WRF fields (Viswanadhapalli et al., 2017). The results of the MITgcm model for the Red Sea have been extensively validated against different data sets and in different environments and applications, as described in Hoteit et al., (2021) and Krokos et al., (2021).

    iv- The normalized monthly oceanic El Niño-Southern Oscillation Index (ONI), East Atlantic/West Russian Pattern

150   (EATL/WRUS), Atlantic Multidecadal Oscillation (AMO), and North Atlantic Oscillation (NAO) time series from 1982 to 2021 were obtained from the National Oceanic and Atmospheric Administration (NOAA) (https://psl.noaa.gov/data/climateindices/list/). The Indian Ocean Dipole (IOD) was downloaded from the Japan Agency for Marine-Earth Science and Technology (JAMSTEC) for the aforementioned period (https://www.jamstec.go.jp/virtualearth/general/en/).

155

    v- Hourly atmospheric data is used to examine the variability of atmospheric conditions in relation to the variability of the SSTA over the entire study period, and used to examine the drivers of the 2010 MHW events, are from the European Center for Medium-Range Weather Forecasts (ECMWF) ERA5 ((Hersbach et al., 2020); https://cds.climate.copernicus.eu/cdsapp#!/dataset/reanalysis-era5-single-levels). The dataset has a spatial resolution

160   of $0.25° \times 0.25°$. The atmospheric fields include the wind components at 10 m altitude (U10 and V10), air temperature at 2 m altitude (T2m), mean sea level pressure (MSLP), shortwave surface net radiation (Q_s), longwave surface net radiation (Q_b), sensible surface heat flux (Q_h), and latent surface heat flux (Q_e). Daily mean values of atmospheric variables were calculated by averaging the hourly data.

2.2 Methods of Analysis

165   MHWs are defined using a variety of methods, each has its advantages and disadvantages. These methods include the use of fixed, relative, or seasonally varying thresholds. In this work, the approach of Hobday et al. (2016, 2018) was used to define and categorize surface MHWs (between 1982 and 2021) and subsurface MHWs (for the February-March 2010 MHW event in the NRS as a case study). Hobday et al. (2016) defined a MHW as an event of unusually high water temperature lasting five consecutive days or longer. During the MHW, water temperature exceeds the 90th percentile climatological threshold.

170   The climatological mean and threshold are calculated in each grid cell for each calendar day of the year using daily water temperature data (at the surface or subsurface levels of the water column) over a 40-year period (1982-2021). Each MHW event can be described by its duration (in days), frequency (in events), mean intensity (in °C), maximum intensity (in °C), cumulative intensity (in °C.days), and total days (in days) (Hobday et al., 2016, 2018). The MATLAB toolbox M_MHW was used to define the MHW metrics (Zhao and Marin, 2019). Annual statistics and time series for MHW frequency were

175   calculated from 1982 to 2021 for each region (whole RS, NRS, and SRS).

SST anomalies were calculated by removing the historical climatological mean (1982-2021) at each grid point from the SST values at the same location. The strong seasonal signal was removed from the SSTA data at each grid cell to obtain a deseasonalized map and time series (Skliris et al., 2012). The warm or cold periods/years were defined as the periods/years that had a strong positive or negative SSTA, respectively. Therefore, the SSTA of the warm/cold years was the average of

180 the SSTAs over those years and the marine heatwave days (MHWDs) for the warm/cold years is the average of the MHWDs over those years. Linear trends in SSTA and MHW frequency are estimated using the least squares method (Wilks, 2019) and their statistical significance is determined using the Modified Mann-Kendall test (MMK) at the 95% confidence level, which takes autocorrelation into account when assessing the significance of the trend (Hamed and Ramachandra Rao, 1998; Wang et al., 2020).

185 To better understand the relationship between the different climate modes (i.e., ONI, EATL/WRUS, AMO, NAO, and IOD) and the occurrence of MHWs over the last four decades in the RS, the correlation maps between them were calculated. The Pearson correlation coefficient (r), the most common method for measuring linear correlations (Kirch, 2008; Patten and Newhart, 2017), was used to calculate the correlation maps, and the significance of these correlations was tested using a two sided t-test (Patten and Newhart, 2017).

190 As a case study, we have focused on MHW events that occurred in 2010, which was an unusual year for both MHWs and climate modes. Therefore, events in this year were defined using the same method used to define long-term MHWs (Hobday et al., 2016). These events were then categorized as moderate (when SST exceeded the threshold), strong (when SST exceeded 2X the threshold), severe (when SST exceeded 3X the threshold by), or extreme (when SST exceeded 4X the threshold) according to the categorization scheme of Hobday et al. (2018). The severe events that occurred between February

195 and March 2010 were then examined in detail. The vertical extent of this event was calculated by computing the MHWs at different levels of the water column (0m, 25m, 55m, 110m and 130m depth). Daily averages of hourly modeled water temperature data were used to calculate the climatology and threshold of the MHW at each water level. The vertical extent of the MHW was then defined by the first depth without MHWs. We also investigated the atmospheric conditions associated with these events using ERA-5 atmospheric data.

200 Following the work of Thomson and Emery (2014) and the description of Nagy et al. (2017, 2021), the net surface heat flux Q_T in W/m^2 was calculated as follows:

$$Q_T = Q_s + Q_b + Q_c + Q_e \,,$$

where Q_s is the heat absorbed by the ocean from incident solar radiation in W/m^2, Q_b is the heat loss from back radiation in W/m^2, Q_c is the sensible heat loss from convection and conduction in W/m^2, and Q_e is the heat loss from evaporation (latent heat) at the ocean surface in W/m^2.

205 heat) at the ocean surface in W/m^2.

3. Results and Discussion

3.1 SST and MHWs characteristics and trends in the Red Sea (1982 – 2021)

The spatial maps of average SST over the entire study period (1982-2021), winter months (January, February and March) and summer months (July, August and September) in RS are shown in Figure 2. The average SST in the Red Sea was
210 between 23 and 28 °C throughout the study period, with a meridional gradient from north to south, with the highest temperatures observed in the SRS and the lowest in the NRS and the Gulfs of Suez and Aqaba (Fig. 2a). In the winter (JFM), the average SST fluctuated between 18 and 27 °C (Fig. 2b), while in the summer (JAS) it fluctuated between 26 and 32 °C (Fig. 2c).

The spatial distribution of the annual mean MHW characteristics of the RS over the last four decades was calculated and
215 shown in Figure 3. The RS exhibits a high spatial variability of MHW characteristics. The mean annual MHW frequency varied between 1.5 and 2.5 events, with the highest mean frequency values recorded in the coastal areas of the SRS and the Strait of Bab El-Mandab (Fig. 3a). The mean duration of the MHW ranged from 8 to more than 20 days (Fig. 3b), with longest MHW duration observed in the NRS and the Gulfs of Suez and Aqaba. The mean and maximum annual MHW intensities (I_{mean} and I_{max}) showed the same pattern of spatial distribution with slightly different magnitudes (Fig. 3c, d). The
220 intense MHWs were observed in the NRS and in the western part of the SRS around Dahlak Kebir Island. In addition, both the mean cumulative MHW intensity (I_{cum}) and the total number of heat days showed a similar pattern of spatial variability (Fig. 3e, f). Figure 3E shows that the mean MHW cumulative intensity varied between 10 and 35 °C.days, with the highest values (> 30 °C. days) found in the NRS and the lowest in the SRS and the Strait of Bab El-Mandab. The mean total MHW days ranged from 20 to over 30 days, with the highest values found in the NRS, coastal areas of the SRS and the Gulfs of
225 Suez and Aqaba. (Fig. 3f). In general, the MHWs in the RS showed different characteristics between the northern and southern basins. The MHWs of the NRS were longer and more intense than those of the SRS, while the MHWs of the SRS were characterized by their frequent occurrence. The same pattern of MHW distribution was also observed by (Bawadekji et al., 2021 and Mohamed et al., 2021).

Spatial trend maps of deseasonalized SST and MHW frequency from 1982 to 2021 in RS are shown in Figure 4. A
230 statistically significant (p < 0.05) trend with a 95% confidence interval was observed across the region. The trends of SST and MHW frequency in the RS are not consistent and ranged from 0.1 to 0.5 °C/decade and 0.5 to 2 events/decade, respectively. The deep water of the RS showed the strongest SST trends (> 0.45 °C/decade; Fig. 4a), and the lowest SST trends were observed in the Strait of Bab El-Mandab and the Gulfs of Suez and Aqaba (< 0.15 °C/decade; Fig. 4a). The highest MHW frequency trends were observed in the SRS and the Gulfs of Suez and Aqaba (> 1.5 event/decade; Fig. 4b),
235 and the lowest trends were observed in the NRS and the Strait of Bab El-Mandab (< 1 event/decade; Fig. 4b). The spatial pattern of MHW trend compared to the spatial distribution and trend of SST indicates that MHW in the Red Sea is driven by SST variability rather than trend.

3.2 SST and MHWs interannual variability

240 The temporal SSTA trends over the study period were 0.33 ± 0.02 °C/decade, 0.34 ± 0.04 °C/decade and 0.32 ± 0.03 °C/decade for the entire RS, NRS and SRS, respectively (Fig. 5). Our results are in good agreement with (Raitsos et al., 2011; Barros et al., 2014; Chaidez et al., 2017; Liu and Yao, 2022). The temporal evolution of SSTA between 1982 and 2021 revealed three distinct SSTA phases of variability: first, from 1982 to 1992, when SSTA was negative on average (cold period); second, between 1993 and 2015, when SSTA fluctuated close to zero (no trend period); and third, when the SSTA

245 anomaly was positive, which was the case in the last six years of the study period from 2016 to 2021 (warm period), which were observed in the entire Red Sea and its sub-basins (Fig. 5). In each period, there were also unusually cold years (i.e. colder than the previous or following year) and warm years (i.e. warmer than the previous or following year). The coldest years were 1985, 1990, 1992, 1993, 1997, 2012 and 2013, while the warmest years were 1991, 1995, 2010 and the last six years of the study period (2016 -2021).

250 The monthly SSTA time series of the RS and its sub-basins show a clear warming that started in 1994 (SSTA ~ 0.5 °C), remained stable a few years later and then almost tripled after 2016 (SSTA > = 1.5 °C; Supplementary Figures S1. a-c). This result is in agreement with Raitsos et al. (2011). Furthermore, the difference between the monthly SSTA of NRS and SRS (S1. d) shows that in the years with generally low SSTA in the Red Sea, NRS was warmer than SRS, while in the years with generally high SSTA in the Red Sea, SRS was warmer than NRS, with the exception of 2010, one of the warmest years in

255 our entire study period. The winter of this year was particularly warm in the NRS (i.e., SSTA difference between NRS and SRS > 1 °C).

In both the warm and cold years, the average SSTA and MHW days (MHWDs) were examined with regard to their spatial distribution. In the cold years, the NRS and the Strait of Bab El-Mandab had the highest SSTA and MHWDs (Fig. 6). In warm years, the SRS and the northern regions of the Gulfs of Suez and Aqaba had the highest SSTA and also the highest

260 number of MHWDs (Fig. 7). 2010 was a unique year among the warm years with a different spatial distribution of SSTA and MHWDs than the other warm years, in which the NRS and the Gulfs of Suez and Aqaba had the highest SSTA and MHWDs (Fig. 8).

The annual variations of MHWs in the RS and its sub-basins during the study period, the annual MHWs for the entire RS, the NRS and the SRS were plotted as shown in Figure 9. The years with the highest MHW frequency were determined using

265 a threshold value, which equals to the mean of the annual MHW frequency plus one standard deviation. Based on this threshold, any year that experienced more than four MHW events was considered to have a high MHW frequency. For the entire RS, the year 2010 and the last five years of the study period had the highest annual MHW frequency (Fig. 9a). The years 2010, 2018, 2019 and 2021 were the years with the highest annual MHW frequency in the NRS (Fig. 9b), while in the SRS the year 1998 and the last five years of the study period had the highest annual MHW frequency (Fig. 9c). It was also

270 found that 78 MHW events occurred in the Red Sea region in the last four decades (1982- 2021), of which 36 (46%) occurred in the last 10 years of the study period. Between 1982 and 2021, a total of 1016 heat days were recorded in the Red

Sea, of which 590 days (58%) occurred in the last decade. These results indicate that the rapid increase in SST in the Red Sea has caused a positive trend in MHWs in the region, and they also suggest that MHWs in the Red Sea are expected to increase in the future with global warming, which is consistent with the findings of (Bawadekji et al., 2021 and Mohamed et

275 al., 2021). A comparison then was made between the atmospheric variables and the annual MHW frequency to provide a general idea of the atmospheric conditions associated with the years with the highest MHW occurrence for the entire RS, NRS and SRS. The annual anomalies of total heat flux (Q_t), air temperature and wind speed are shown in S2 – S4 in the Supplementary Figures. The high MHW frequency was accompanied by an anomalously high Q_t, which is particularly evident in 2010 in the NRS and 1998 in the SRS (S2). This high heat flux was caused by the anomalously high air

280 temperature observed in the same years (S3). Since the wind in these years was not sufficient to support the cooling of the SST (S4), this excess heat absorbed by the ocean from the atmosphere likely led to the formation of several MHW events in the above mentioned years.

3.3 Climate modes and MHWs in the Red Sea

To investigate the possible relationship between the climate indices, the annual SSTA and the annual MHW frequency in the

285 RS over the last 4 decades, a correlation analysis was performed and its significance was tested with a 95% confidence interval. Based on the calculated correlations between the NOAA modes and the annual SSTA and MHW frequency, only the modes that showed a significant correlation ($p < 0.05$) with the SSTA and/or MHW frequency are discussed in this section, as shown in Figure 10.

The AMO index showed a high significant correlation (> 0.7) with SSTA and MHW frequency across the Red Sea (Figs. 10a

290 and b). The relationship between AMO and SST in the Red Sea was also investigated by Krokos et al. (2019), who reported that a long-term AMO oscillation modulates the SST trends in the Red Sea and that the recorded trends in the Red Sea coincide with a positive phase of the AMO. The second climate mode that was positively correlated with both SSTA and MHW frequency was the IOD index with a correlation between 0.2 and 0.4, showing a stronger influence on SRS (Figs. 10c and d). A strong negative correlation was observed between the EATL/WRUS index and both SSTA and MHW frequency

295 (Figs. 10e and f). This correlation was strongest in the NRS and in the deepest part of the Red Sea (i.e. the RS deep water is mainly formed in the NRS by the Red Sea Deep Water (RSDW) thermohaline cell (Hoteit et al., 2021)). So far, no study has attempted to investigate the relationship between the Red Sea SST and the EATL/WRUS climate mode which were already performed by Hamdeno and Alvera-Azcaráte (2023) in the Mediterranean Sea. The later study reported a negative correlation between them, especially in the Levantine Basin and the Aegean Sea (Eastern Mediterranean (EM Basin)). This

300 is consistent with our study, as they found that the EATL/WRUS correlates mainly with the EM basin, which is geographically close to RS and connected to the NRS through the Suez Canal. The NAO index showed a negative correlation with the SSTA and affected the NRS more than the SRS with a correlation coefficient of less than -0.3. The correlation between the NAO and MHW frequency was not significant except in the SRS with a positive correlation of 0.2 and in the Gulfs of Suez and Aqaba with a negative correlation of -0.2 (Figs. 10g and h). The ONI showed a negative

305   correlation with the SSTA, which was more pronounced in the coastal areas of the central and southern RS. These are the same areas that showed a significant negative correlation between ONI and the frequency of MHWs (Figs. 10i and j).

The time series of the different climate modes and the annual frequency of MHWs were compared and presented in Figure. 11. Good agreement was found between the AMO time series and the annual MHW frequency. The years with the lowest MHW frequency (1982 - 1994) coincided with a negative AMO phase, while on the other hand the years with a high MHW

310   frequency also experienced a strong positive AMO phase (Fig. 11a). In addition, the IOD time series also showed a correspondence with the annual MHW frequency, especially between 1982 and 1993, where the IOD had on average a negative phase coinciding with a low MHW frequency, while in the last 7 years of the study period (2015 - 2021) the high MHW frequencies coincided with the positive phase of the IOD (Fig. 11b). The negative correlation between the EATL/WRUS index and the frequency of MHWs is also observed when comparing their annual time series. Figure 11c

315   shows that the years with low MHW frequency coincided with the positive phase of the EATL/WRUS index and vice versa. The comparison between the NAO and ONI indices with the annual time series of MHW frequency (Figs. 11d and e) did not suggest a clear relationship between their occurrence, which could also be seen in the correlation maps (Figs. 10 e - h), as the correlation was not significant in most parts of the Red Sea.

In the last four decades, the year 2010 showed the highest MHW frequency, which coincided with one of the strongest

320   positive AMO phases (i.e. the AMO is positively correlated with the MHW frequency), while at the same time EATL/WRUS and NAO had their strongest negative phases during the entire study period (meaning that, EATL/WRUS and NAO are negatively correlated with the MHW frequency).

3.4 Case Study: 2010 MHWs in the Northern Red Sea

The study of SSTs and MHWs and their relationship to the various climate indices has highlighted 2010 as an exceptional

325   year in the entire record. Therefore, in this section focuses on the MHWs that occurred in the NRS in 2010, their spatial and vertical extent, and the atmospheric conditions during their occurrence to gain a better understanding of their forcing and properties. The NRS was affected by ten MHWs during both the winter and summer of 2010. The MHW event that occurred between February and March was the most extreme (highest intensity with a SSTA of about 4 °C above climatology), peaking on March 12, 2010 (Fig. 12). The vertical extent of this MHW event compared to the MLD and MHW at different

330   depth levels (surface, 25 m, 55 m, 110 m, and 130 m) was calculated, and the results are shown in Figure 13. It was observed that the regular sub-daily cycle of water temperature (i.e., high temperature during the day and low temperature during the night) gradually disappeared during the days of MHW and was completely absent during the peak days of the event. This suggests that the ocean temperature reached the limit where the usual cooling during the night was insufficient to lower the high SSTA, and this heat was stored in the water column for the duration of the event. In addition, upper layer temperature

335   and MLD showed a strong negative relationship (i.e., a thin mixed layer coincided with the days of the highest water temperature) with a time lag between the drop in MLD and the high water temperature of about 4 days, suggesting that a sharp drop in MLD contributed to the rise in temperatures, especially in the surface layers of the water column. Our analysis

also showed that the temperature anomaly extended vertically into the water column at about 120 m depth during the MHW event (Fig. 13b - f). Moreso, the duration of the MHW event varied from the surface to the subsurface. For example, the

340 duration at the surface (9 February to 18 March) was shorter than the duration at 25 m and 55 m depth (9 February to 31 March), implying that the heat of the MHW event was stored longer in the middle layer than at the surface. At 110 m depth, the duration of the MHW was shorter (February 26 to March 17) than in the upper layers and occurred around the peak day of the surface event, indicating that the higher the SSTA, the deeper the MHW event could penetrate into the water column.

A combination of atmospheric conditions were found to be associated with the MHW event (Fig. 14). During the MHW

345 event, SSTA increased in the NRS and was about 4 °C above the climatology average (Fig. 14b), which was associated with an increase in air temperature (Tair) of about 6 °C relative to before the MHW event, particularly over the western African countries (Egypt, Eritrea, and Ethiopia) and along the coast of Saudi Arabia (Fig. 14e). This increase in Tair led to an increase in Qt (up to 100 W/m2), indicating that the ocean was absorbing heat from the atmosphere, and this was more evident in the NRS (Fig. 14h). The average MSLP maps showed an opposite distribution of Tair, so that MSLP was

350 relatively lower during the MHW event compared to its values before the MHW event (Fig. 14j-l). Before the MHW event, winds blew from the eastern part of the study area (i.e., from the regions that had the highest MSLP on those days) and blew mainly toward the southern Red Sea (Fig. 14m). On the days of the MHW, winds in the eastern part of the study area (inland Saudi Arabia) blew from a southerly to northerly direction, while winds on the Red Sea blew from a southerly direction and veered off to the west before reaching the NRS region (i.e., the area hit by the MHW), and there was almost no wind on the

355 NRS (Fig. 14n). In summary, our results show that this severe MHW event is due to the large amount of heat absorbed by the ocean from the atmosphere, the shallow mixed layer and the lake of cooling caused by the absence of wind.

4. Conclusions

The explicit impacts of global warming on ocean temperatures are evident and contribute to both the overall temperature rise and the exacerbation of extremes. Here, we focused on understanding the spatio-temporal variability of MHWs in the Red

360 Sea from 1982 to 2021. We investigated their annual variability in the different RS regions. Their relationships with different climate indices were also explored. A particular focus of this study is a detailed analysis of the extreme MHW events of 2010 in the NRS.

By analyzing satellite-derived SSTs, we found a consistent warming trend in the Red Sea since the mid-1990s, with a notable increase after 2016. This increasing SST trend is related to an increase in MHWs throughout the Red Sea. Over the

365 past four decades, we have identified 78 MHW events totalling 1016 heat days in the RS region. Remarkably, 46% of these events and 58% of the heat days have occurred in the last decade, indicating an acceleration in the occurrence of MHWs in the RS. When examining the spatial characteristics of MHWs, we found different spatial patterns between the MHWs in the NRS and the SRS. In the NRS, MHWs occur longer and more intense, while they occur more frequently in the SRS. When looking at the time series of the annual frequency of MHWs across the Red Sea, we found that the highest annual

370   frequencies occurred in 2010 and in the last five years of our study. These frequent MHWs were associated with
anomalously high Qt, which is particularly caused by the anomalously high air temperature and insufficient winds to support
the cooling of the SST observed in the same years. Our study highlights the exceptional character of 2010, in which we
observe a unique distribution of SSTA and marine heatwave days (MHWDs). While high SSTA and MHWDs in warm years
are typically found in the SRS, 2010 breaks the trend with the highest values ever recorded in the NRS. In addition, the

375   increased MHW frequency in 2010 is consistent with a strong positive phase of the Atlantic Multidecadal Oscillation (AMO)
and the Indian Ocean Dipole (IOD). At the same time, it coincides with pronounced negative phases of the East
Atlantic/West Russia pattern (EATL/WRUS) and the North Atlantic Oscillation (NAO), which makes the climate dynamics
even more complex. In 2010, ten MHW events occurred in the NRS, both in winter and summer. The most intense event
occurred in February-March with an SSTA of about 4°C above the climatology extending vertically to 120 meters. This

380   extreme event coincided with minimal winds over the affected region and a 6°C rise in air temperature, resulting in a
significant increase in heat flux (Qt, up to 100 W/m²).

The Red Sea is a unique and diverse marine ecosystem with high biodiversity and plays an important role in the economies
of surrounding countries, supporting fishing, tourism and other industries. The potential changes in the spatial patterns of
MHWs in the Red Sea, affecting different regions that are considered potential refugia for coral reefs in a warming climate,

385   suggest the need to understand the mechanisms that drive MHWs and their impacts on marine life in the Red Sea. This
knowledge is essential for effective conservation and management strategies and crucial for predicting and mitigating
potential economic losses, as well as for developing adaptation measures to preserve local livelihoods. In addition, research
on MHWs in the Red Sea region will enable the generation of new scientific knowledge and help to fill gaps in the existing
literature and advance marine science. For future work, the compound between MHWs and other extreme events will be

390   investigated and their impact on the Red Sea ecosystem will also be studied across borders.

395

400 **5. References**

Amaya, D. J., Miller, A. J., Xie, S.-P., and Kosaka, Y. (2020). Physical drivers of the summer 2019 North Pacific marine heatwave. *Nat Commun* 11, 1903. doi: 10.1038/s41467-020-15820-w

Arafeh-Dalmau, N., Montaño-Moctezuma, G., Martínez, J. A., Beas-Luna, R., Schoeman, D. S., and Torres-Moye, G. (2019). Extreme Marine Heatwaves Alter Kelp Forest Community Near Its Equatorward Distribution Limit. *Front.*
405 *Mar. Sci.* 6, 499. doi: 10.3389/fmars.2019.00499

Bamston, A. G., Chelliah, M., and Goldenberg, S. B. (1997). Documentation of a highly ENSO-related sst region in the equatorial pacific: Research note. *Atmosphere-Ocean* 35, 367–383. doi: 10.1080/07055900.1997.9649597

Barale, V. (2014). "The African Marginal and Enclosed Seas: An Overview," in *Remote Sensing of the African Seas* , eds. V. Barale and M. Gade (Dordrecht: Springer Netherlands), 3–29. doi: 10.1007/978-94-017-8008-7_1

410 Barnston, A. G., and Livezey, R. E. (1987). Classification, Seasonality and Persistence of Low-Frequency Atmospheric Circulation Patterns. *Monthly Weather Review* 115, 1083–1126. doi: 10.1175/1520-0493(1987)115<1083:CSAPOL>2.0.CO;2

Barros, V. R., Field, C. B., Dokken, D. J., Mastrandrea, M. D., and Mach, K. J. eds. (2014). *Climate Change 2014: Impacts, Adaptation and Vulnerability: Working Group II Contribution to the IPCC Fifth Assessment Report of the*
415 *Integovernmental Panel on Climate Change*. Cambridge: Cambridge University Press. doi: 10.1017/CBO9781107415386

Bawadekji, A., Tonbol, K., Ghazouani, N., Becheikh, N., and Shaltout, M. (2021). General and Local Characteristics of Current Marine Heatwave in the Red Sea. *JMSE* 9, 1048. doi: 10.3390/jmse9101048

Behera, S. K., Doi, T., and Ratnam, J. V. (2021). "5 - Air–sea interactions in tropical Indian Ocean: The Indian Ocean
420 Dipole," in *Tropical and Extratropical Air-Sea Interactions* , ed. S. K. Behera (Elsevier), 115–139. doi: 10.1016/B978-0-12-818156-0.00001-0

Bjerknes, J. (1969). ATMOSPHERIC TELECONNECTIONS FROM THE EQUATORIAL PACIFIC. *Monthly Weather Review* 97, 163–172. doi: 10.1175/1520-0493(1969)097<0163:ATFTEP>2.3.CO;2

Bower, A. S., and Farrar, J. T. (2015). "Air–Sea Interaction and Horizontal Circulation in the Red Sea," in *The Red Sea*
425 Springer Earth System Sciences. , eds. N. M. A. Rasul and I. C. F. Stewart (Berlin, Heidelberg: Springer Berlin Heidelberg), 329–342. doi: 10.1007/978-3-662-45201-1_19

Cai, W., Wang, G., Li, Z., Zheng, X., Yang, K., and Ng, B. (2021). "Chapter 21 - Response of the positive Indian Ocean dipole to climate change and impact on Indian summer monsoon rainfall," in *Indian Summer Monsoon Variability* , eds. J. Chowdary, A. Parekh, and C. Gnanaseelan (Elsevier), 413–432. doi: 10.1016/B978-0-12-822402-1.00010-7

430 Carlson, D. F., Yarbro, L. A., Scolaro, S., Poniatowski, M., McGee-Absten, V., and Carlson, P. R. (2018). Sea surface temperatures and seagrass mortality in Florida Bay: Spatial and temporal patterns discerned from MODIS and AVHRR data. *Remote Sensing of Environment* 208, 171–188. doi: 10.1016/j.rse.2018.02.014

Chaidez, V., Dreano, D., Agusti, S., Duarte, C. M., and Hoteit, I. (2017). Decadal trends in Red Sea maximum surface temperature. *Sci Rep* 7, 8144. doi: 10.1038/s41598-017-08146-z

435   Chefaoui, R. M., Duarte, C. M., and Serrão, E. A. (2018). Dramatic loss of seagrass habitat under projected climate change in the Mediterranean Sea. *Glob Change Biol* 24, 4919–4928. doi: 10.1111/gcb.14401

Chen, W. Y., and Dool, H. V. den (2003). Sensitivity of Teleconnection Patterns to the Sign of Their Primary Action Center. *Monthly Weather Review* 131, 2885–2899. doi: 10.1175/1520-0493(2003)131<2885:SOTPTT>2.0.CO;2

Diaz-Almela, E., Marbà, N., and Duarte, C. M. (2007). Consequences of Mediterranean warming events in seagrass
440   (Posidonia oceanica) flowering records. *Global Change Biol* 13, 224–235. doi: 10.1111/j.1365-2486.2006.01260.x

Dool, H. M. van den, Saha, S., and Johansson, Å. (2000). Empirical Orthogonal Teleconnections. *Journal of Climate* 13, 1421–1435. doi: 10.1175/1520-0442(2000)013<1421:EOT>2.0.CO;2

Eakin, C. M., Morgan, J. A., Heron, S. F., Smith, T. B., Liu, G., Alvarez-Filip, L., et al. (2010). Caribbean Corals in Crisis: Record Thermal Stress, Bleaching, and Mortality in 2005. *PLOS ONE* 5, e13969. doi:
445   10.1371/journal.pone.0013969

Eladawy, A., Nadaoka, K., Negm, A., Abdel-Fattah, S., Hanafy, M., and Shaltout, M. (2017). Characterization of the northern Red Sea's oceanic features with remote sensing data and outputs from a global circulation model. *Oceanologia* 59, 213–237. doi: 10.1016/j.oceano.2017.01.002

Garrabou, J., Coma, R., Bensoussan, N., Bally, M., Chevaldonné, P., Cigliano, M., et al. (2009). Mass mortality in
450   Northwestern Mediterranean rocky benthic communities: effects of the 2003 heat wave. *Global Change Biology* 15, 1090–1103. doi: 10.1111/j.1365-2486.2008.01823.x

Genevier, L. G. C., Jamil, T., Raitsos, D. E., Krokos, G., and Hoteit, I. (2019). Marine heatwaves reveal coral reef zones susceptible to bleaching in the Red Sea. *Glob Change Biol* 25, 2338–2351. doi: 10.1111/gcb.14652

Good, S., Fiedler, E., Mao, C., Martin, M. J., Maycock, A., Reid, R., et al. (2020). The Current Configuration of the OSTIA
455   System for Operational Production of Foundation Sea Surface Temperature and Ice Concentration Analyses. *Remote Sensing* 12, 720. doi: 10.3390/rs12040720

Hamdeno, M., and Alvera-Azcaráte, A. (2023). Marine heatwaves characteristics in the Mediterranean Sea: Case study the 2019 heatwave events. *Front. Mar. Sci.* 10, 1093760. doi: 10.3389/fmars.2023.1093760

Hamdeno, M., Nagy, H., Ibrahim, O., and Mohamed, B. (2022). Responses of Satellite Chlorophyll-a to the Extreme Sea
460   Surface Temperatures over the Arabian and Omani Gulf. *Remote Sensing* 14, 4653. doi: 10.3390/rs14184653

Hamed, K. H., and Ramachandra Rao, A. (1998). A modified Mann-Kendall trend test for autocorrelated data. *Journal of Hydrology* 204, 182–196. doi: 10.1016/S0022-1694(97)00125-X

Hersbach, H., Bell, B., Berrisford, P., Hirahara, S., Horányi, A., Muñoz-Sabater, J., et al. (2020). The ERA5 global reanalysis. *Q.J.R. Meteorol. Soc.* 146, 1999–2049. doi: 10.1002/qj.3803

465   Hobday, A. J., Alexander, L. V., Perkins, S. E., Smale, D. A., Straub, S. C., Oliver, E. C. J., et al. (2016). A hierarchical approach to defining marine heatwaves. *Progress in Oceanography* 141, 227–238. doi: 10.1016/j.pocean.2015.12.014

Hobday, A., Oliver, E., Sen Gupta, A., Benthuysen, J., Burrows, M., Donat, M., et al. (2018). Categorizing and Naming Marine Heatwaves. *Oceanog* 31. doi: 10.5670/oceanog.2018.205

470 Hoerling, M. P., Kumar, A., and Xu, T. (2001). Robustness of the Nonlinear Climate Response to ENSO's Extreme Phases. *Journal of Climate* 14, 1277–1293. doi: 10.1175/1520-0442(2001)014<1277:ROTNCR>2.0.CO;2

Holbrook, N. J., Scannell, H. A., Sen Gupta, A., Benthuysen, J. A., Feng, M., Oliver, E. C. J., et al. (2019). A global assessment of marine heatwaves and their drivers. *Nat Commun* 10, 2624. doi: 10.1038/s41467-019-10206-z

Holbrook, N. J., Sen Gupta, A., Oliver, E. C. J., Hobday, A. J., Benthuysen, J. A., Scannell, H. A., et al. (2020). Keeping
475 pace with marine heatwaves. *Nat Rev Earth Environ* 1, 482–493. doi: 10.1038/s43017-020-0068-4

Hoteit, I., Abualnaja, Y., Afzal, S., Ait-El-Fquih, B., Akylas, T., Antony, C., et al. (2021). Towards an End-to-End Analysis and Prediction System for Weather, Climate, and Marine Applications in the Red Sea. *Bulletin of the American Meteorological Society* 102, E99–E122. doi: 10.1175/BAMS-D-19-0005.1

Huang, B., Thorne, P. W., Banzon, V. F., Boyer, T., Chepurin, G., Lawrimore, J. H., et al. (2017). Extended Reconstructed
480 Sea Surface Temperature, Version 5 (ERSSTv5): Upgrades, Validations, and Intercomparisons. *Journal of Climate* 30, 8179–8205. doi: 10.1175/JCLI-D-16-0836.1

Hughes, T. P., Anderson, K. D., Connolly, S. R., Heron, S. F., Kerry, J. T., Lough, J. M., et al. (2018). Spatial and temporal patterns of mass bleaching of corals in the Anthropocene. *Science* 359, 80–83. doi: 10.1126/science.aan8048

Karnauskas, K. B., and Jones, B. H. (2018). The Interannual Variability of Sea Surface Temperature in the Red Sea From 35
485 Years of Satellite and In Situ Observations. *Journal of Geophysical Research: Oceans* 123, 5824–5841. doi: 10.1029/2017JC013320

Kirch, W. ed. (2008). "Pearson's Correlation Coefficient," in *Encyclopedia of Public Health* (Dordrecht: Springer Netherlands), 1090–1091. doi: 10.1007/978-1-4020-5614-7_2569

Krokos, G., Cerovecki, I., Zhan, P., Hendershott, M., and Hoteit, I. (2021). *Seasonal Evolution of Mixed Layers in the Red*
490 *Sea and the Relative Contribution of Atmospheric Buoyancy and Momentum Forcing*.

Krokos, G., Papadopoulos, V. P., Sofianos, S. S., Ombao, H., Dybczak, P., and Hoteit, I. (2019). Natural Climate Oscillations may Counteract Red Sea Warming Over the Coming Decades. *Geophysical Research Letters* 46, 3454–3461. doi: 10.1029/2018GL081397

Le Grix, N., Zscheischler, J., Laufkötter, C., Rousseaux, C. S., and Frölicher, T. L. (2021). Compound high-temperature and
495 low-chlorophyll extremes in the ocean over the satellite period. *Biogeosciences* 18, 2119–2137. doi: 10.5194/bg-18-2119-2021

Liu, X., and Yao, F. (2022). Relationship of the Warming of Red Sea Surface Water over 140 Years with External Heat Elements. *Journal of Marine Science and Engineering* 10, 846. doi: 10.3390/jmse10070846

Marshall, J., Adcroft, A., Hill, C., Perelman, L., and Heisey, C. (1997). A finite-volume, incompressible Navier Stokes
500 model for studies of the ocean on parallel computers. *Journal of Geophysical Research: Oceans* 102, 5753–5766. doi: 10.1029/96JC02775

McPhaden, M. J., Zebiak, S. E., and Glantz, M. H. (2006). ENSO as an Integrating Concept in Earth Science. *Science* 314, 1740–1745. doi: 10.1126/science.1132588

Mohamed, B., Nagy, H., and Ibrahim, O. (2021). Spatiotemporal Variability and Trends of Marine Heat Waves in the Red
505 Sea over 38 Years. *JMSE* 9, 842. doi: 10.3390/jmse9080842

Nagy, H., Elgindy, A., Pinardi, N., Zavatarelli, M., and Oddo, P. (2017). A nested pre-operational model for the Egyptian shelf zone: Model configuration and validation/calibration. *Dynamics of Atmospheres and Oceans* 80, 75–96. doi: 10.1016/j.dynatmoce.2017.10.003

Nagy, H., Mohamed, B., and Ibrahim, O. (2021). Variability of Heat and Water Fluxes in the Red Sea Using ERA5 Data (1981–2020). *Journal of Marine Science and Engineering* 9, 1276. doi: 10.3390/jmse9111276

Oliver, E. C. J., Benthuysen, J. A., Darmaraki, S., Donat, M. G., Hobday, A. J., Holbrook, N. J., et al. (2021). Marine Heatwaves. *Annu. Rev. Mar. Sci.* 13, 313–342. doi: 10.1146/annurev-marine-032720-095144

Oliver, E. C. J., Donat, M. G., Burrows, M. T., Moore, P. J., Smale, D. A., Alexander, L. V., et al. (2018). Longer and more frequent marine heatwaves over the past century. *Nat Commun* 9, 1324. doi: 10.1038/s41467-018-03732-9

Patten, M. L., and Newhart, M. (2017). *Understanding Research Methods: An Overview of the Essentials*. 10th ed. Tenth edition. | New York, NY : Routledge, 2017.: Routledge. doi: 10.4324/9781315213033

Pujol, C., Pérez-Santos, I., Barth, A., and Alvera-Azcárate, A. (2022). Marine Heatwaves Offshore Central and South Chile: Understanding Forcing Mechanisms During the Years 2016-2017. *Front. Mar. Sci.* 9, 800325. doi: 10.3389/fmars.2022.800325

Raitsos, D., Hoteit, I., Prihartato, P., Chronis, T., Triantafyllou, G., and Abualnaja, Y. (2011). Abrupt warming of the Red Sea. *Geophysical Research Letters - GEOPHYS RES LETT* 38. doi: 10.1029/2011GL047984

Rivetti, I., Fraschetti, S., Lionello, P., Zambianchi, E., and Boero, F. (2014). Global Warming and Mass Mortalities of Benthic Invertebrates in the Mediterranean Sea. *PLOS ONE* 9, e115655. doi: 10.1371/journal.pone.0115655

Schenke, H.-W. (2013). "GEBCO," in *Encyclopedia of Marine Geosciences* , eds. J. Harff, M. Meschede, S. Petersen, and J. Thiede (Dordrecht: Springer Netherlands), 1–2. doi: 10.1007/978-94-007-6644-0_63-3

Schneider, D. P., Deser, C., Fasullo, J., and Trenberth, K. E. (2013). Climate Data Guide Spurs Discovery and Understanding. *Eos Trans. AGU* 94, 121–122. doi: 10.1002/2013EO130001

Semenov, V. A., Latif, M., Dommenget, D., Keenlyside, N. S., Strehz, A., Martin, T., et al. (2010). The Impact of North Atlantic–Arctic Multidecadal Variability on Northern Hemisphere Surface Air Temperature. *Journal of Climate* 23, 5668–5677. doi: 10.1175/2010JCLI3347.1

Sen Gupta, A., Thomsen, M., Benthuysen, J. A., Hobday, A. J., Oliver, E., Alexander, L. V., et al. (2020). Drivers and impacts of the most extreme marine heatwave events. *Sci Rep* 10, 19359. doi: 10.1038/s41598-020-75445-3

Shaltout, M. (2019). Recent sea surface temperature trends and future scenarios for the Red Sea. *Oceanologia* 61, 484–504. doi: 10.1016/j.oceano.2019.05.002

Shukla, J. (1998). Predictability in the Midst of Chaos: A Scientific Basis for Climate Forecasting. *Science* 282, 728–731. doi: 10.1126/science.282.5389.728

Skliris, N., Sofianos, S., Gkanasos, A., Mantziafou, A., Vervatis, V., Axaopoulos, P., et al. (2012). Decadal scale variability of sea surface temperature in the Mediterranean Sea in relation to atmospheric variability. *Ocean Dynamics* 62, 13–30. doi: 10.1007/s10236-011-0493-5

540 Smale, D., and Wernberg, T. (2009). Satellite-derived SST Data as a Proxy for Water Temperature in Nearshore Benthic Ecology. *ECU Publications* 387. doi: 10.3354/meps08132

Thomson, R. E., and Emery, W. J. (2014). *Data Analysis Methods in Physical Oceanography*. Elsevier. doi: 10.1016/C2010-0-66362-0

Trisos, C. H., Merow, C., and Pigot, A. L. (2020). The projected timing of abrupt ecological disruption from climate change.
545 *Nature* 580, 496–501. doi: 10.1038/s41586-020-2189-9

Visbeck, M. H., Hurrell, J. W., Polvani, L., and Cullen, H. M. (2001). The North Atlantic Oscillation: Past, present, and future. *Proceedings of the National Academy of Sciences* 98, 12876–12877. doi: 10.1073/pnas.231391598

Viswanadhapalli, Y., Dasari, H. P., Langodan, S., Challa, V. S., and Hoteit, I. (2017). Climatic features of the Red Sea from a regional assimilative model. *Intl Journal of Climatology* 37, 2563–2581. doi: 10.1002/joc.4865

550 Wang, F., Shao, W., Yu, H., Kan, G., He, X., Zhang, D., et al. (2020). Re-evaluation of the Power of the Mann-Kendall Test for Detecting Monotonic Trends in Hydrometeorological Time Series. *Frontiers in Earth Science* 8. Available at: https://www.frontiersin.org/article/10.3389/feart.2020.00014 (Accessed March 10, 2022).

Weatherall, P., Marks, K. M., Jakobsson, M., Schmitt, T., Tani, S., Arndt, J. E., et al. (2015). A new digital bathymetric model of the world's oceans. *Earth and Space Science* 2, 331–345. doi: 10.1002/2015EA000107

555 Wilks, D. S. (2019). *Statistical Methods in the Atmospheric Sciences*. Elsevier. doi: 10.1016/C2017-0-03921-6

Zhang, R. (2007). Anticorrelated multidecadal variations between surface and subsurface tropical North Atlantic. *Geophysical Research Letters* 34. doi: 10.1029/2007GL030225

Zhao, Z., and Marin, M. (2019). A MATLAB toolbox to detect and analyze marine heatwaves. *JOSS* 4, 1124. doi: 10.21105/joss.01124

560

Funding:

This work benefits financial support of the Aspirant F.R.S.-FNRS (Fonds de la Recherche Scientifique de Belgique, Communauté Française de Belgique) through funding the position of AB and funding a Aspirant - ASP grant.

Conflict of interest:

565 The authors declare that the research was conducted in the absence of any commercial or financial relationships that could be construed as a potential conflict of interest. Some authors are members of the editorial board of journal Ocean Science.

Figures:

570

595
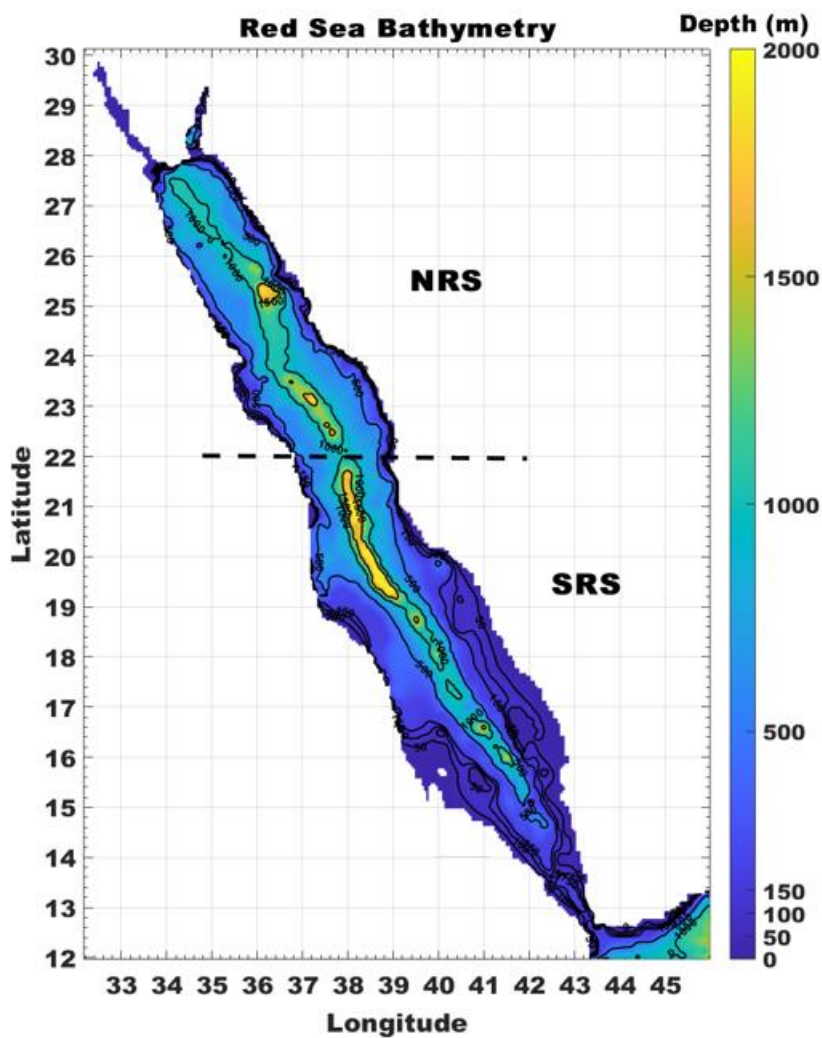
Figure 1. Bathymetry map of the Red Sea. Bathymetry corresponds to the GEBCO bathymetry dataset (www.gebco.net).

600
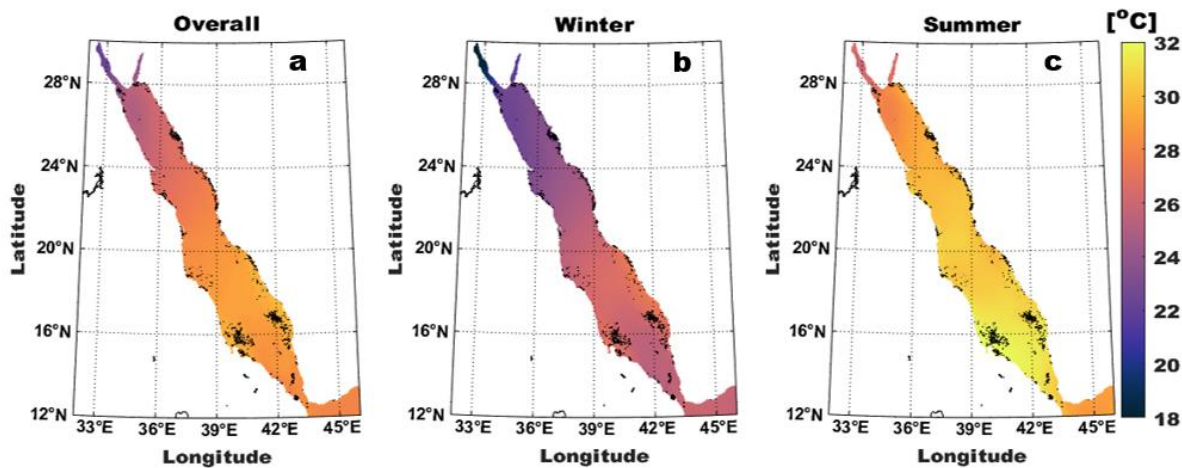
Figure 2. The spatial distribution of average Red Sea SST (in ºC) from 1982 to 2021. (a) over the entire study period, (b) during winter (January, February, and March), and (c) during summer (July, August, and September).
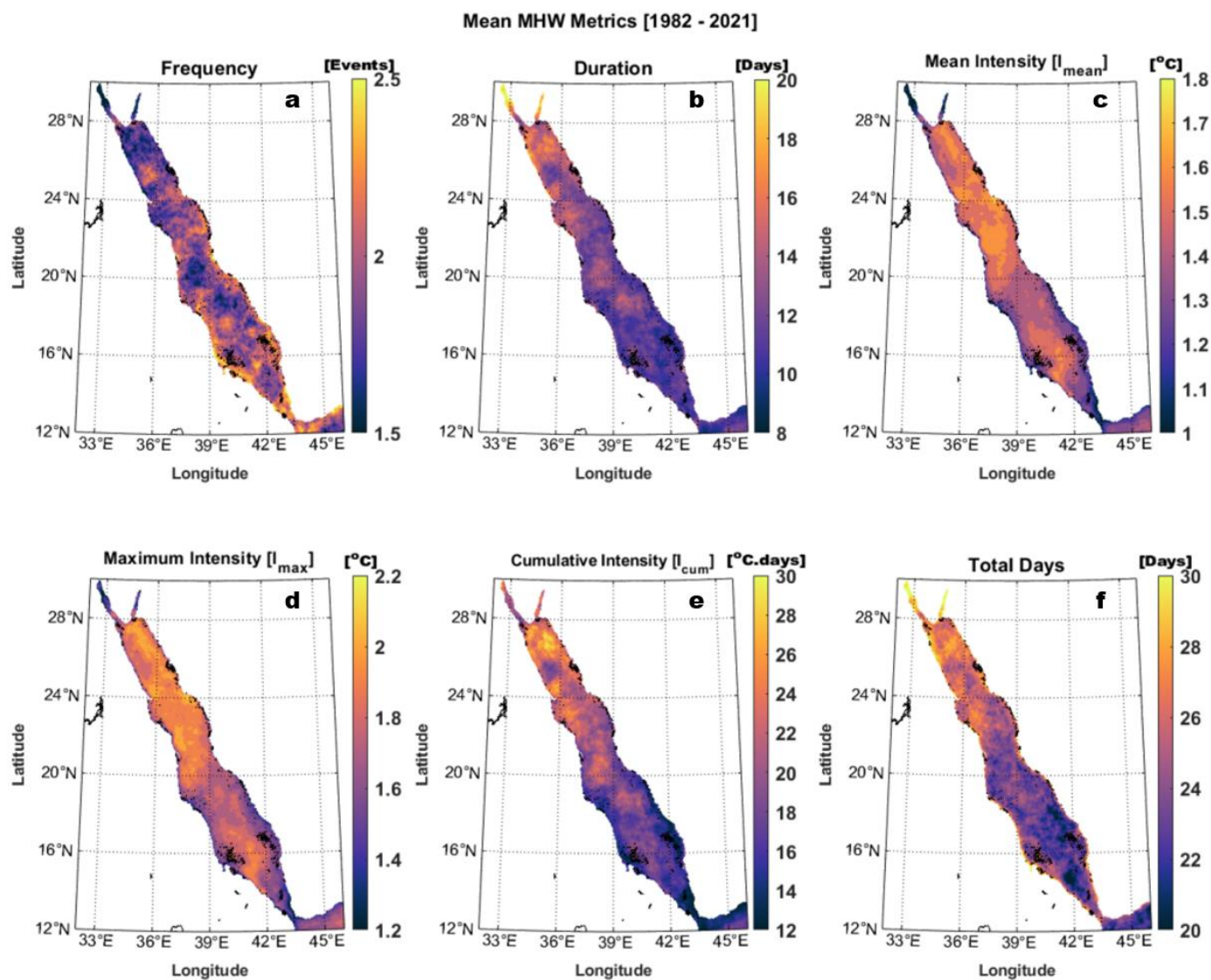
Figure 3. The spatial distribution of average MHWs characteristics at RS between 1982 and 2021. The average MHWs frequency (a), duration (b), mean intensity (c), maximum intensity (d), cumulative intensity (e), and total days (f).

640
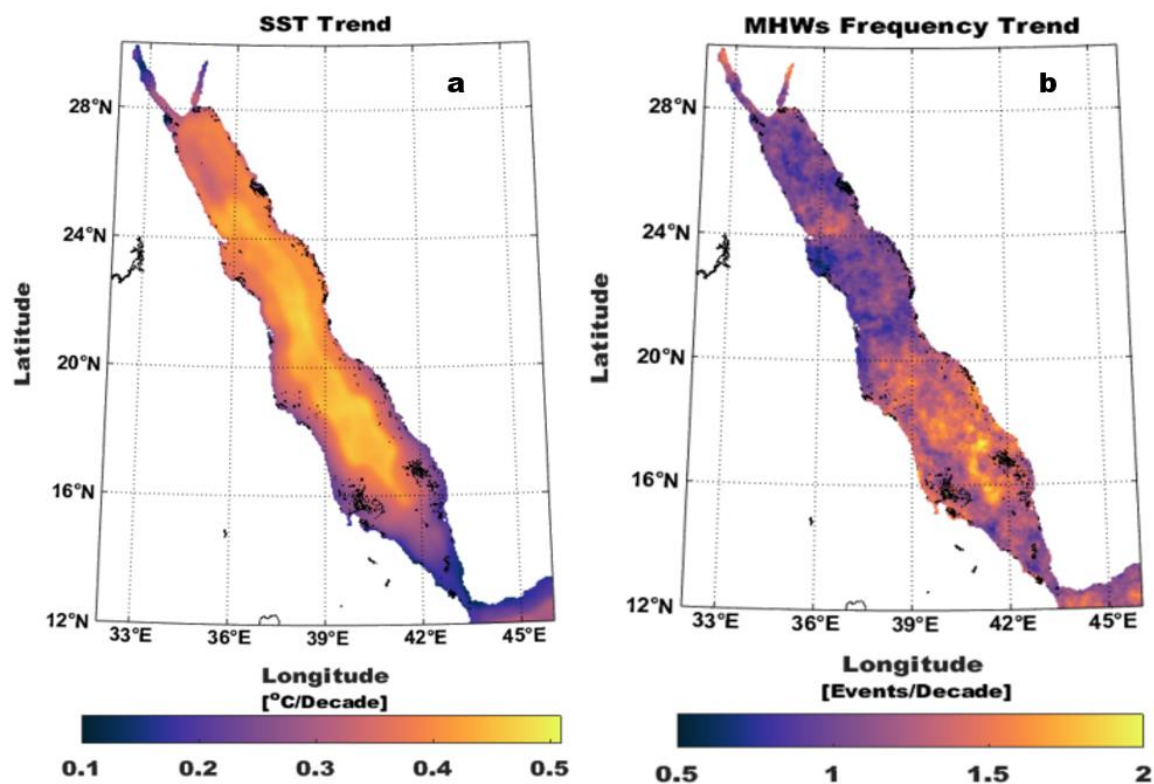
Figure 4. The spatial distribution of (a) SST (in ºC/decade) and (b) MHWs frequency (in Event/decade) trends in the Red Sea from 1982 to 2021.
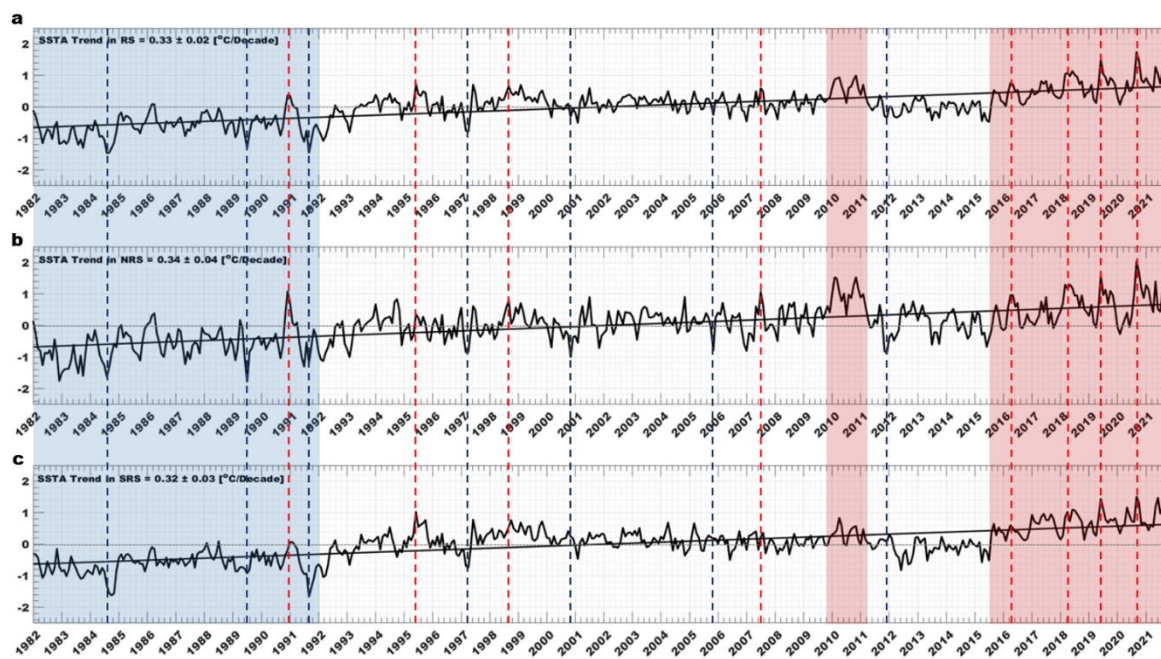
Figure 5. The temporal evolution and trend of the SST anomaly (in °C) in the entire Red Sea (a), northern Red Sea (b), and southern Red Sea (c) between 1982 and 2021. The blue and red shaded areas represent the cold and warm periods, respectively, within the study period. The blue and red dotted lines represent the coldest and warmest years, respectively, within the study period.

715
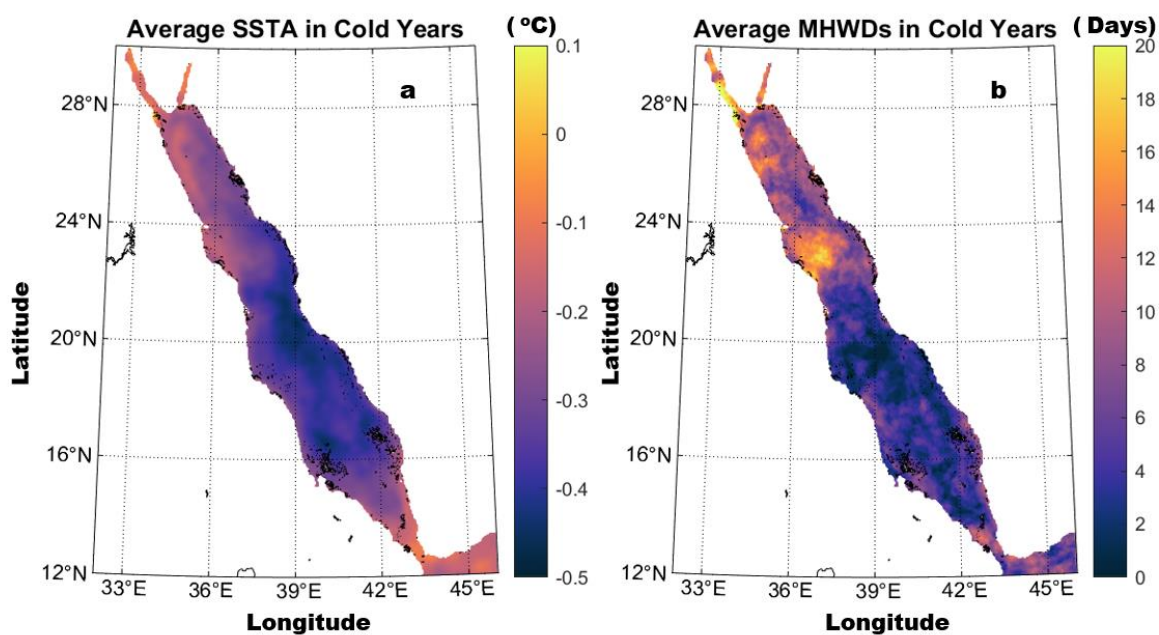
Figure 6. The spatial distribution of the average (a) SST anomaly (in °C) and (b) MHW days (in Days) in the Red Sea during
720   the cold years of the study period (1982-2021).

725

730

735
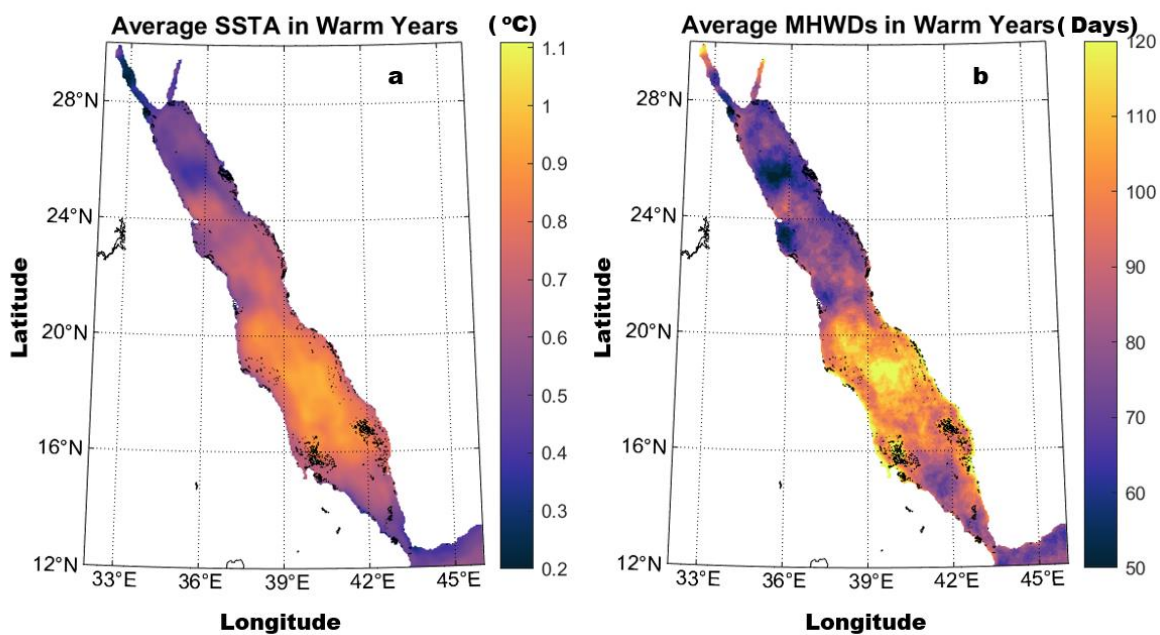
Figure 7. The spatial distribution of the average (a) SST anomaly (in ºC) and (b) MHW days (in Days) in the Red Sea during the warm years of the study period (1982-2021).

740

745
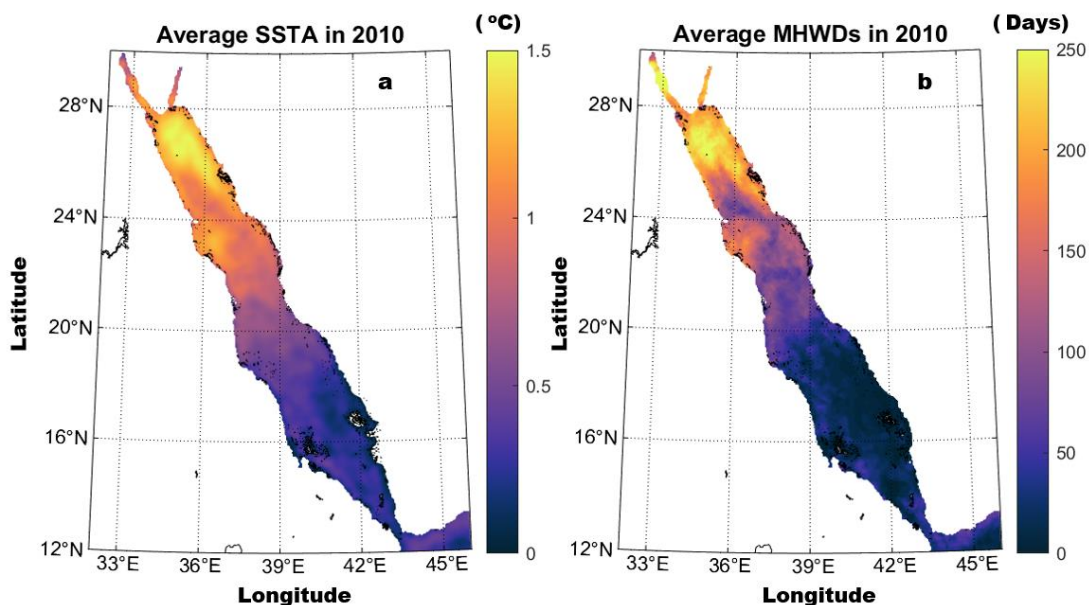
750

Figure 8. The spatial distribution of the average (a) SST anomaly (in °C) and (b) MHW days (in Days) in the Red Sea in 2010.
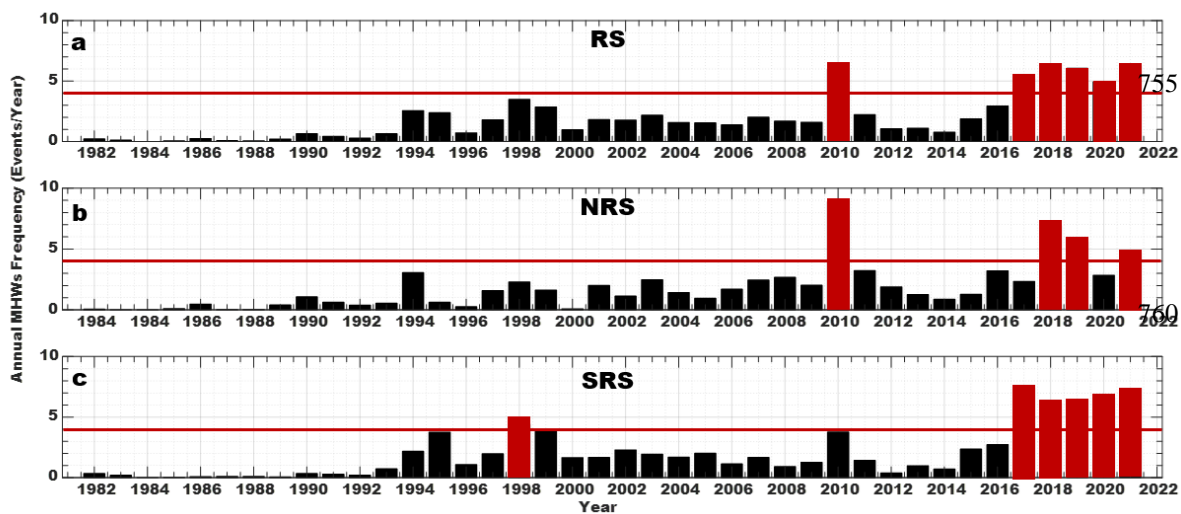
765

Figure 9. Interannual variability of MHWs frequency in the entire Red Sea (a), northern Red Sea (b), and southern Red Sea (c) between 1982 and 2021. The red bars represent the years with the highest MHWs frequency in each basin

770
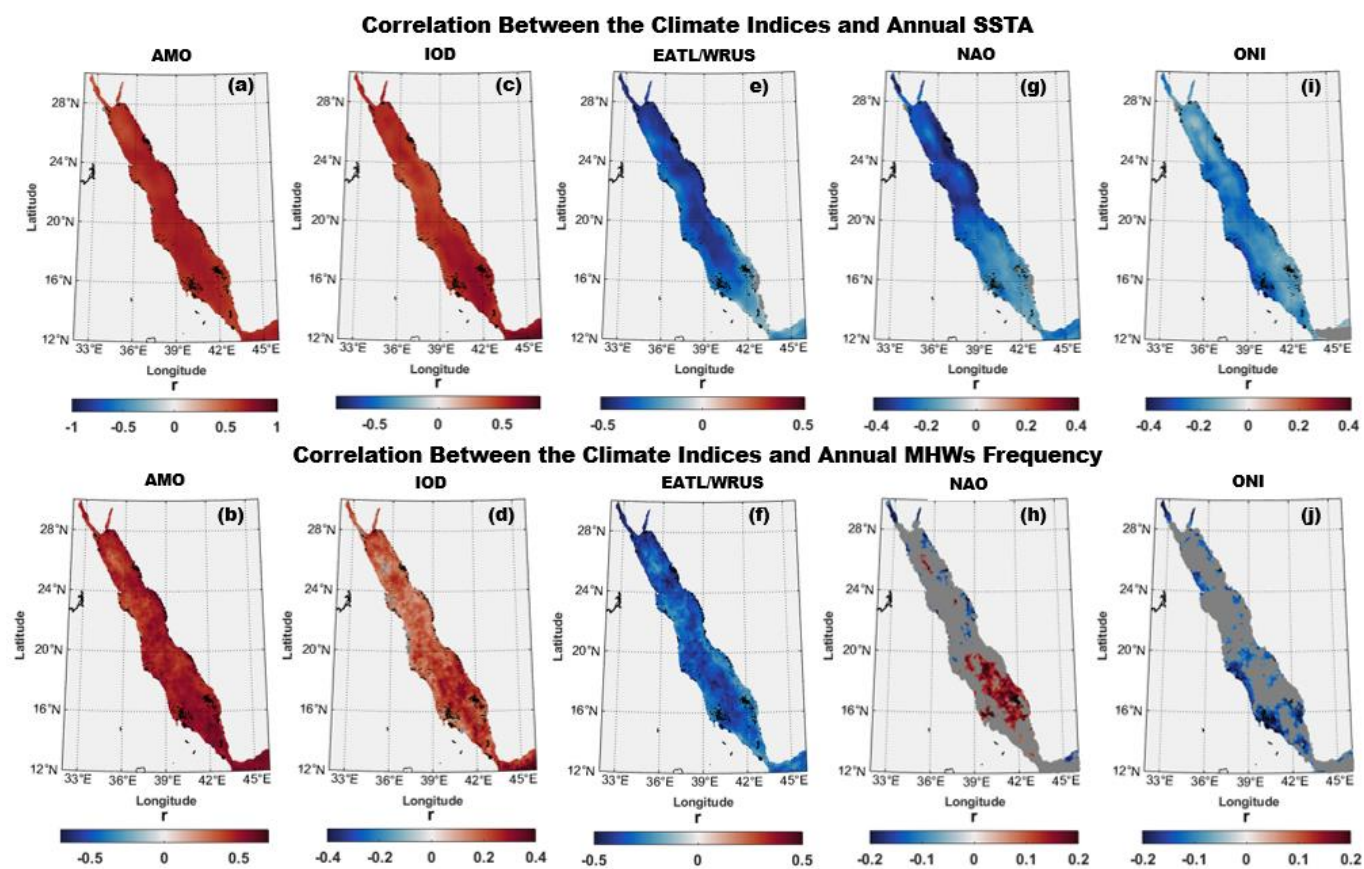
Figure 10. Correlation maps of the different climate modes with the SST anomaly (upper panels) and the frequency of MHWs (lower panels) in the Red Sea from 1982 to 2020, correlating with AMO index (a, b), IOD pattern (c, d), NAO index (e, f), ONI index (g, h), and EATL/WRUS index (i, j). The gray color on the maps indicates where the correlation is not significant ($P_{val} > 0.05$).
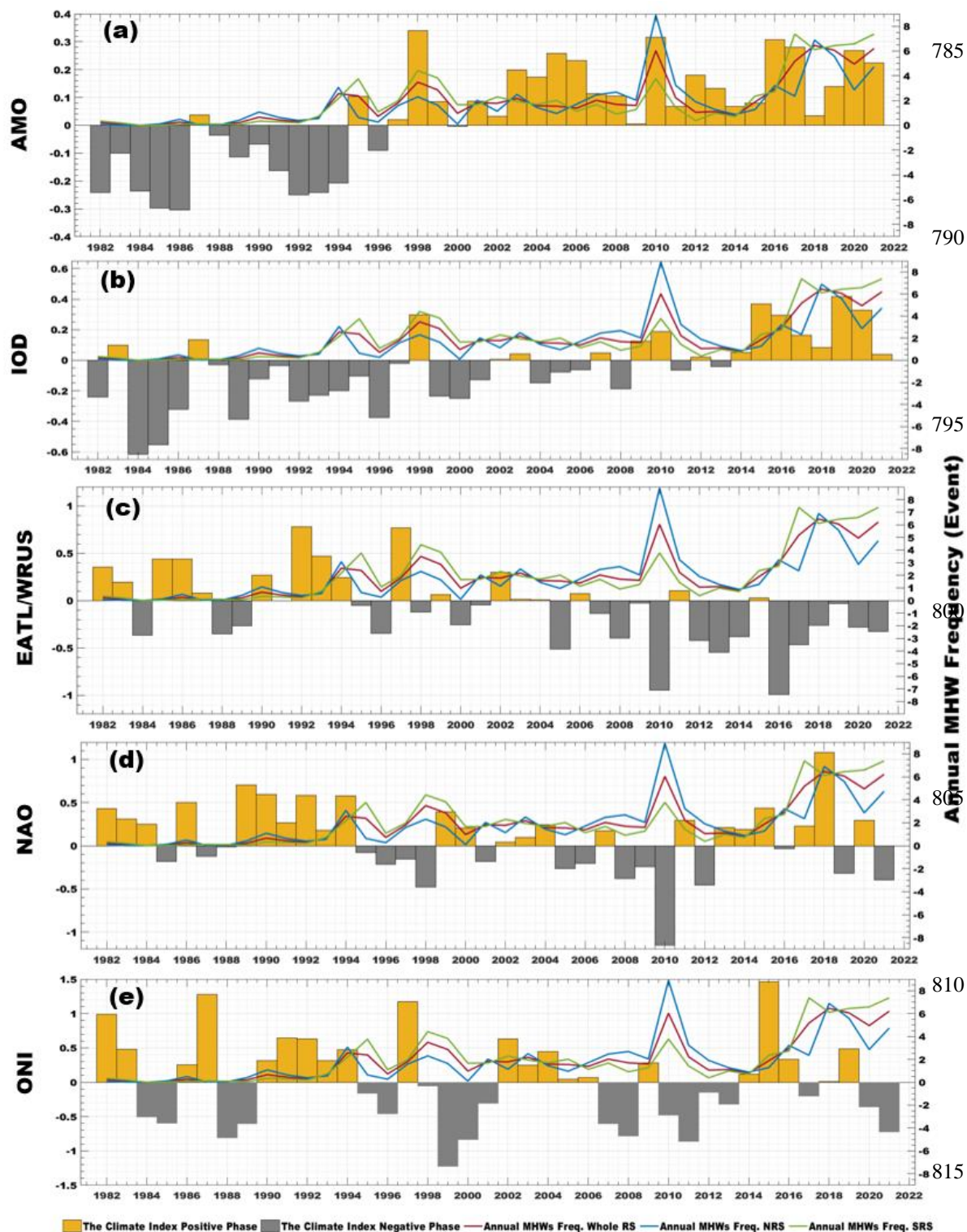
780

Figure 11. The annual time series of normalized AMO index (a), IOD index (b), EATL/WRUS pattern (c), NAO index (d), and ONI index (e) with annual MHWs frequency in the entire Red Sea (red line), NRS (blue line), and SRS (green line). The

820 orange and gray shading refer to the positive and negative phases of the climate indices, respectively.
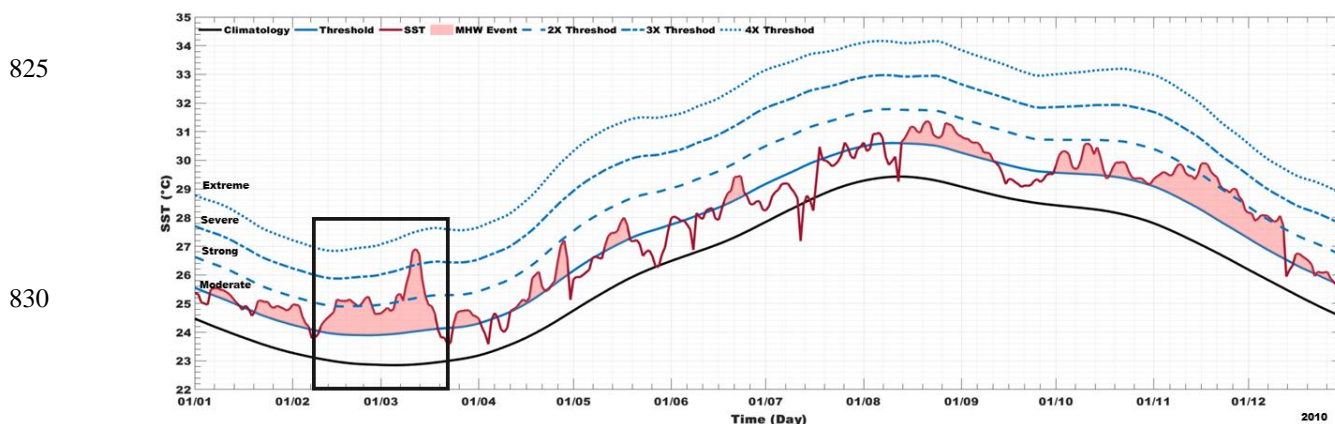
835 Figure 12. The MHW events that occurred in the NRS in 2010. The red shaded area refers to the MHW event. The red solid line represents the SST, the black solid line represents the climatology, the blue solid line represents the threshold, and the blue dotted lines are the multiples of the threshold (define the MHW categories). The MHW categories are moderate (when the SST exceeds the threshold), strong (when the SST exceeds 2 times the threshold), severe (when the SST exceeds 3 times the threshold), or extreme (when the SST exceeds 4 times the threshold)

840

845
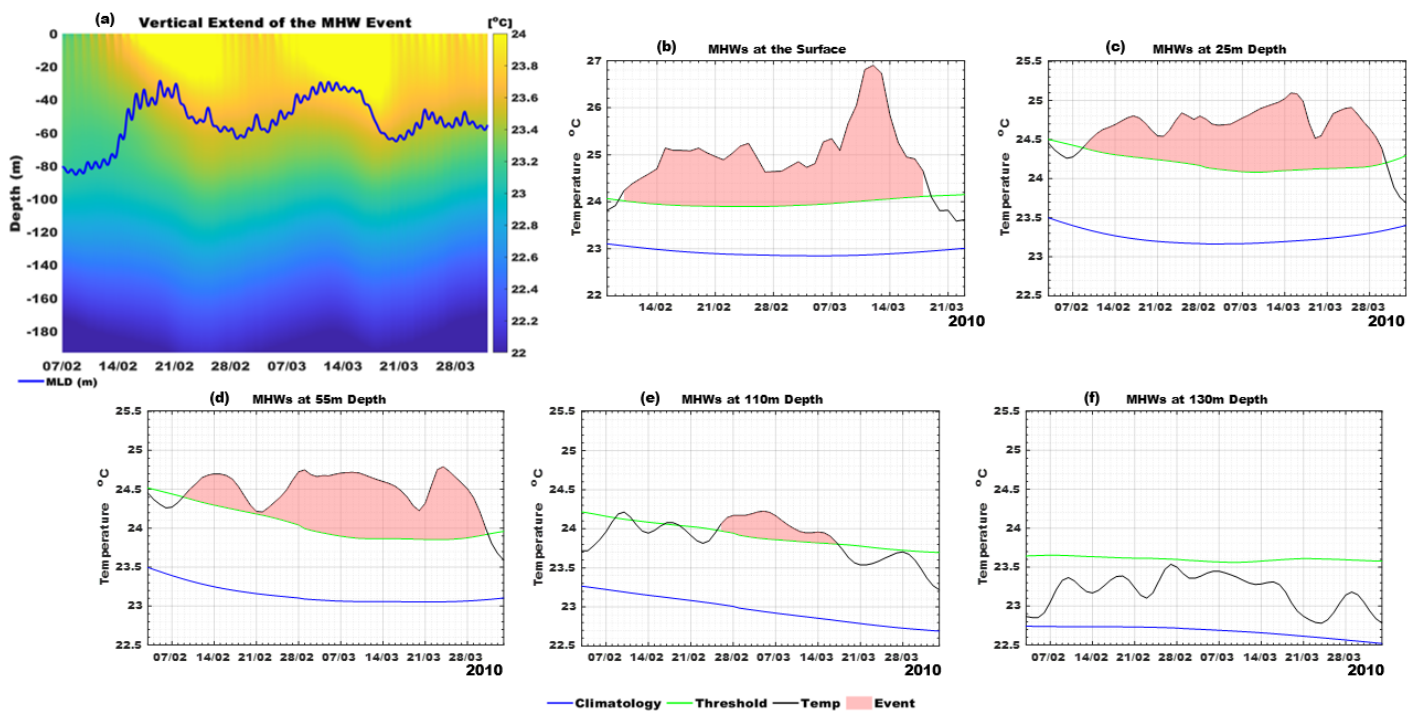
Figure 13. The MHW event occurred in the NRS between February and March 2010. The vertical extent (a), the blue line on panel (a) represents the MLD. Panels (b - f) represent the MHWs at the different water column depths (surface, 25m, 55m, 110m, and 130m), the red shaded area is the MHW event, the black solid line is the SST, the blue solid line is the climatology mean, and the green solid line is the 90th percentile threshold.

865
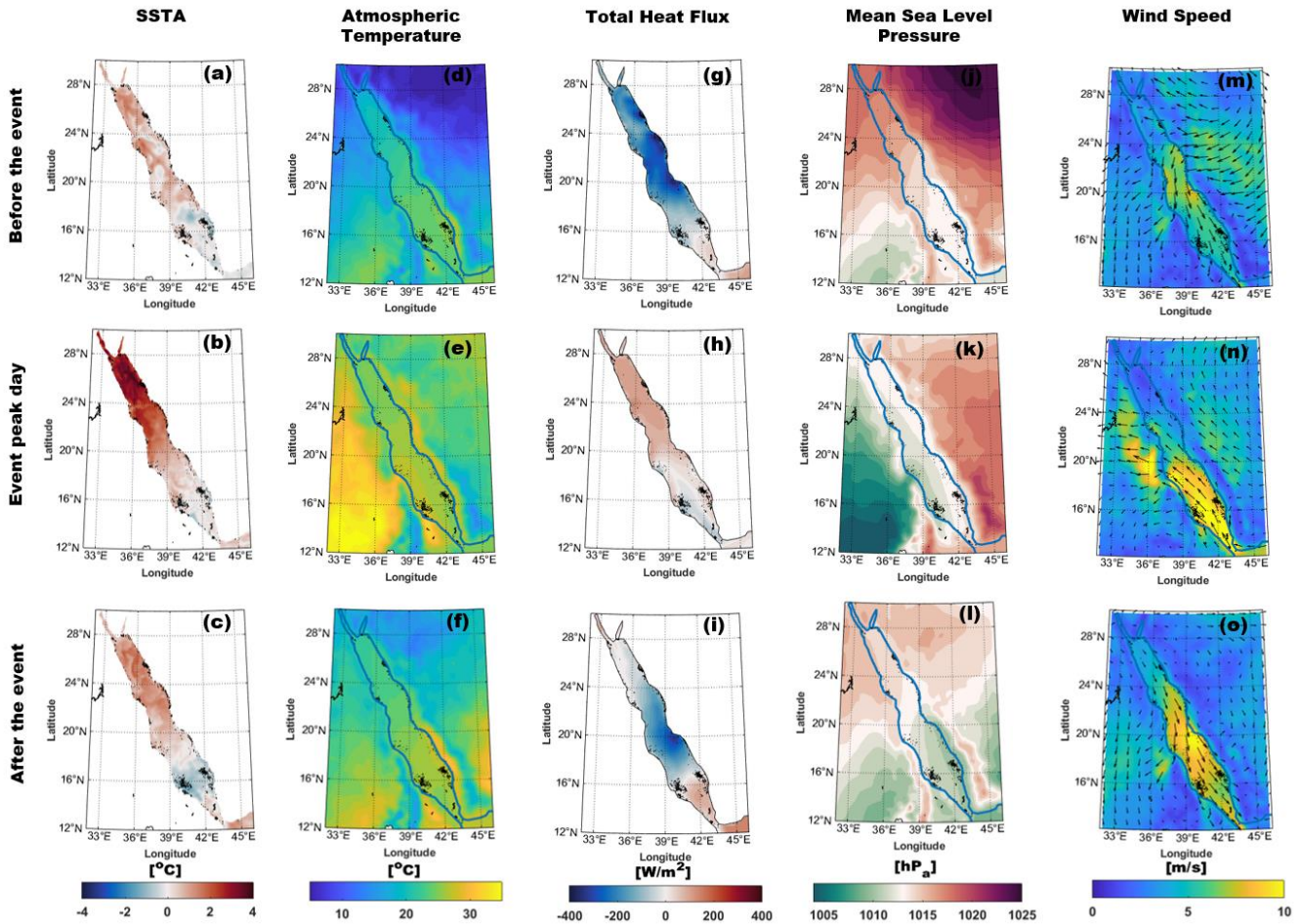
Figure 14. The average spatial distribution of atmospheric variables before the MHW event (from 3rd to 7th of February) on the upper panels, during the MHW event (from 10th to 15th of March) on the middle panels and after the MHW event (from 20th to 25th of March) on the lower panels. Panels (a - c) represent SSTA (in °C), panels (d - f) represent atmospheric temperature (in °C), panels (g - i) represent total heat flux (in W/m^2), panels (j - l) represent mean sea level pressure (in hPa), and panels (m - o) represent wind speed (in m/s) and wind direction.

875